Analyst

Accepted Manuscript

This article can be cited before page numbers have been issued, to do this please use: A. C. Soares, J. C. Soares, F. M. Shimizu, V. D. C. Rodrigues, I. T. Awan, M. E. Melendez, M. H. D. O. Piazzetta, A. L. Gobbi, R. M. Reis, J. H. T. G. Fregnani, A. L. Carvalho and O. N. Oliveira Jr., *Analyst*, 2018, DOI: 10.1039/C8AN00430G.

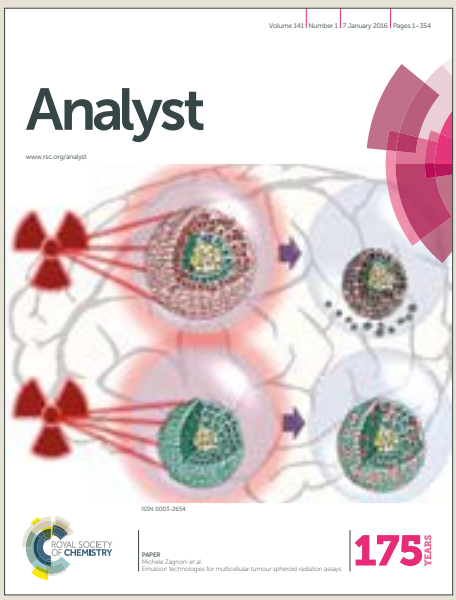

View Article Online
DOI: 10.1039/C8AN00430G

Analyst

ARTICLE

A simple architecture with self-assembled monolayers to build immunosensors for detecting the pancreatic cancer biomarker CA19-9

Received
Accepted

DOI: 10.1039/x0xx00000x

www.rsc.org/

Andrey Coatrini Soares*[a,b], Juliana Coatrini Soares [a], Flavio Makoto Shimizu [a,c], Valquiria da Cruz Rodrigues [a], Iram Taj Awan [a], Matias Eliseo Melendez [d], Maria Helena Oliveira Piazzetta [c], Angelo Luiz Gobbi [c], Rui Manuel Reis [d,e,f], José Humberto T. G. Fregnani [d], André Lopes Carvalho [d] and Osvaldo N. Oliveira Jr [a].

The challenge of early diagnosis of pancreatic cancer in routine clinical practice requires low-cost means of detection, and this may be achieved with immunosensors based on electrical or electrochemical principles. In this paper, we report on a potentially low-cost immunosensor built with interdigitated gold electrodes coated with a self-assembled monolayer and a layer of anti-CA19-9 antibodies, which is capable of detecting the pancreatic cancer biomarker CA19-9 using electrical impedance spectroscopy. Owing to specific, irreversible adsorption of CA19-9 onto its corresponding antibody, according to data from polarization-modulated infrared reflection absorption spectroscopy (PM-IRRAS), the immunosensor is highly sensitive and selective. It could detect CA19-9 in commercial samples with a limit of detection of 0.68 U/mL, in addition to distinguishing between blood serum samples from patients with different concentrations of CA19-9. Furthermore, treating the capacitance data with information visualization methods we were able to verify the selectivity and robustness of the immunosensor with regard to false positives, as the samples containing higher CA19-9 concentrations, including from tumor cells, could be distinguished from those with possible interferents.

Introduction

Early diagnosis is crucial for increasing survival rates and life expectancy for cancer patients, particularly for pancreatic cancer for which clinical symptoms are normally inexistent before the tumor is at an advanced stage[1]. The challenge is then to provide low-cost point-of-care methods for routine blood or urine tests, which requires identification of suitable biomarkers. For pancreatic cancer, the antigen CA19-9, a glycoprotein synthesized by human pancreatic and biliary duct cells[2], is frequently used as a clinical biomarker[3]. Because there is a corresponding specific antibody, immunosensors can be built and CA19-9 is usually detected with the Enzyme Linked Immuno Sorbent Assay (ELISA). This method, however, involves high cost and has limited sensitivity that may hamper its use for detecting cancer at early stages[4]. This has motivated significant research into immunosensors based on electrochemical and impedance spectroscopy principles of detection[5,6]. These sensors are made with films of materials organized at the nanoscale where organized, tailored structures lead to successful nanotechnologies[7]. Typically, these nanostructures contain a suitable matrix for effective immobilization of the antibodies, and are fabricated with experimental techniques that allow for control of molecular architectures[8]. Examples of such techniques are the Langmuir-Blodgett (LB)[9], layer-by-layer (LbL)[10–12] and the self-assembled monolayer (SAM)[13,14] techniques, which assist in preserving the structural integrity of biomolecules and communication with electrodes[12,15].

In developing these immunosensors, the main goals have been associated with seeking synergy in the materials chosen for the matrix and in the identification of the detection method, including data analysis, in order to yield high sensitivity and selectivity toward CA19-9. Examples of film architectures include chitosan/concanavalin A[16], poly(ethyleneimine)/carbon nanotubes[8,17], carbon-based materials[8], electrospun nanofibers[18] and polythionine-Au

[a] São Carlos Institute of Physics, University of São Paulo, São Carlos, Brazil.
[b] Department of Materials Engineering, São Carlos School of Engineering, University of São Paulo, São Carlos, Brazil.
[c] Brazilian Nanotechnology National Laboratory, Brazilian Center for Research in Energy and Materials, Campinas, Brazil.
[d] Molecular Oncology Research Center, Barretos Cancer Hospital, Barretos, Brazil.
[e] Life and Health Sciences Research Institute (ICVS), School of Health Sciences, University of Minho, Braga, Portugal.
[f] ICVS/3B's - PT Government Associate Laboratory, Braga/Guimarães, Portugal.

Electronic Supplementary Information (ESI) available: Cyclic Voltammograms for film architectures, AFM images of functionalized electrodes, Calibration curves obtained from PM-IRRAS spectra, Parallel coordinates plot for the capacitance spectra of CA19-9 commercial samples and tables of quantifications of cells and patients samples. See DOI: 10.1039/x0xx00000x

View Article Online
DOI: 10.1039/C8AN00430G

composites[19]. While the combination of nanomaterials in some cases provides superior performance, incorporation of various components turns the fabrication procedures more complex and expensive. As for detection, methods related to electrochemistry[18,20,21], chemiluminescence[22], piezoelectricity[23], surface plasmon resonance[24,25] and impedance spectroscopy[17,26] have been used.

In this study, we produced immunosensors with one of the simplest architectures possible to immobilize the anti-CA19-9 antibodies, i.e. the sensing units had the active layer adsorbed on a SAM activated with N-hydroxisuccinimide (NHS) and ethyl-3-(3-dimethyllaminopropyl) carbodiimide(EDC). In spite of this simplicity, the immunosensing performance was competitive with similar, more sophisticated sensors. Indeed, compared to previous contributions[16–18], including from our own group, the novelty in the present study lies mainly in the fabrication of a potentially low-cost immunosensor with simpler architecture that is able not only to detect low concentrations of CA19-9 in commercial samples, but also distinguish between blood serum samples from patients of a cancer hospital with varied CA19-9 concentrations. This was made possible by treating the impedance spectroscopy data with information visualization methods[27–29], which have not been exploited to the extent they should in the biosensing field.

Experimental

Electrode Modification.

Detection of CA19-9 protein was performed with an immunosensor made with an active layer of anti-CA19-9 (Aviva System Biology, USA) deposited on a self-assembled monolayer (SAM) of 11-mercaptoundecanoic acid (11-MUA) on gold interdigitated electrodes fabricated onto BK7 substrates. The electrodes had 50 pairs of fingers, 10 µm wide and spaced 10µm away from each other. Deposition of 11-MUA was made by immersing the interdigitated electrode into a 5mmol/L solution for 8h, followed by activation of the 11-MUA carboxylic acid groups by immersion into 0.1 M N-hydroxisuccinimide (NHS) (Sigma-Aldrich, USA) and 0.1 M ethyl-3-(3-dimethyllaminopropyl) carbodiimide(EDC) (Sigma-Aldrich, USA) for 30 min. A layer of anti-CA19-9 was adsorbed by immersion in 20µL of antibody solution at 37ºC during 45 min, and the biosensor architecture was completed by immersion into an aqueous solution of 1% bovine serum albumin (BSA) (Sigma-Aldrich, USA) to block non-specific active sites. After each step, electrodes were washed with ethanol and ultrapure water to remove non-adsorbed molecules. Figure 1 shows a schematic picture of the immunosensor architecture.

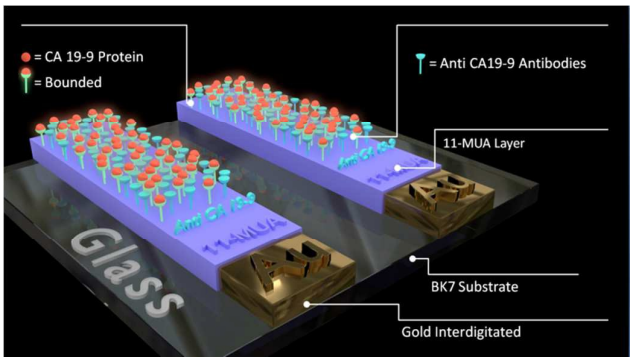

Figure 1: Immunosensor architecture containing an 11-MUA monolayer and immobilized antibodies for detecting the CA19-9 protein.

Film Characterization.

The nanostructured films used to functionalize the electrodes were characterized using cyclic voltammetry and atomic force microscopy (AFM). Cyclic voltammetry, in particular, was used to optimize the fabrication conditions for the matrix layer of 11-MUA. Gold electrodes (~0.25 cm^2) were immersed in 11-MUA solution for 1, 8, 12 and 24 h, washed in ethanol to remove non-adsorbed molecules, dried for 2h at 25ºC and placed in the electrochemical cell, which had an Ag/AgCl reference electrode and platinum counter electrode (0.5 cm^2). A sweep potential was applied between −0.2 V and 0.7 V at a scan rate of 50 mV/s in 5 mmol/L $[Fe(CN)6]^{-3}$/$[Fe(CN)6]^{-4}$ solution. All measurements were carried out with a potentiostat Autolab PGSTAT 204 (Metrohm, Switzerland). An AFM instrument from Bruker (USA), model Dimension FastScan, was used to investigate the morphology of the nanostructured films deposited on the interdigitated electrodes in the tapping mode with scan rate of 0.6 Hz.

Detection of CA19-9 Protein

The CA19-9 protein (Aviva System Biology, USA) was detected using electrical impedance spectroscopy with a Solartron model SI 1260 A (Solartron Analytical, USA), in the range between 10^2 and 10^6Hz, with immunosensors built as described above. Immunosensors were first exposed to CA19-9 commercial samples at 37 U/mL during 0, 1, 2, 4, 6, 8, 10, 12, 14 and 15 min to optimize the adsorption time of the biomarkers. Then different concentrations of CA19-9 commercial samples (0, 0.1, 4, 6, 16, 41, 78, 115, 152 and 189 U/mL) were dropped on the functionalized electrodes, followed by washing in ultrapure water and immersion in a phosphate buffered saline (PBS) solution to acquire the capacitance spectra. The data collected were used to construct the calibration curves and calculate the limit of detection. A series of control experiments was performed with ascorbic acid (AA) (Sigma-Aldrich, USA), uric acid (UA) (Sigma-Aldrich, USA), biomarker p24 (p24) (Bio-Synthesis Inc, USA), CA19-9 in fetal bovine serum (FBS) and two cell lines supernatant

View Article Online
DOI: 10.1039/C8AN00430G

samples, HT-29 (containing 12.26 U/mL of CA19-9) and SW-620 (with no detectable levels of CA19-9). These cell lines, obtained from Barretos Cancer Hospital, were maintained in Dulbecco's modified eagle's medium (DMEM) and RPMI 1640, containing 10% fetal bovine serum (FBS), 1% penicillin/streptomycin and 2 mM glutamine in a humidified 5% CO2 incubator at 37 °C. PBS buffer was used to wash the cells lines, followed by cultivation in OptiMEM media, without serum. After 48 h, the supernatant was filtered and stored at −80°C for further quantification of CA19-9. For gold-standard quantification, we use an electrochemiluminescence immunoassay (ECLIA) in a commercially available kit in Cobas601 (Roche Diagnostics, USA). The calibration curve was calculated with Elecsys CA19−9 CalSet (Roche Diagnostics, USA).

Samples from eight patients diagnosed with pancreatic cancer were also analyzed using electrical impedance measurements. The immunosensor was immersed in the serum of eight patients, with unknown CA19-9 concentration, during 10 min for CA19-9 protein adsorption. The characteristics of the patient samples are summarized in Table S1 in Electronic Supplementary Material.

Information Visualization for Biosensing.

Biosensing data are commonly treated using statistical methods that reduce their dimensionality, with Principal Component Analysis (PCA)[30] being perhaps the most common method. Optimization of immunosensing performance may be reached by applying other information visualization methods that allow for a detailed evaluation of the data, especially when feature selection is desired. For sensors based on impedance spectroscopy this is particularly relevant because the electrical response varies significantly with the frequency of the applied field, and sensing events may occur preferably at specific frequency ranges. Indeed, when sensing depends on changes of the electrical double layer formed at a solid/liquid interface on a charged surface, the low frequency region (100 Hz or less) is the most relevant. Here we processed the capacitance spectra using a free software suite referred to as PEx-Sensors[29], which implements projection techniques that use interactive maps in 2-D (IDMAP) and parallel coordinates (PC)[31].In the PC technique[32], the dataset is plotted on equally spaced coordinate axes scaled to depict the range of measured values. Capacitance values are inferred from the intersection of the value measured with the frequency axis, generating a visual representation that reveals the distribution of the data and their correlations[29]. We also used IDMAP which considers Euclidean distances between the signals of different samples X = {x_1, x_2, x_3, …,x_n) and projects these data instances into a lower-dimension space, where Y = {y_1, y_2, y_3, …, y_n) is the position of visual elements. For IDMAP, the error functions are calculated using an injective function, which considers the maximum $\delta_{\max}$ and minimum $\delta_{\min}$ distances between data instances, the distance between two samples in original space $\delta(x_i, x_j)$ and the distance function on the projected space $d(y_i, y_j)$. This function minimizes the term $|\delta(x_i, x_j) - d(f(x_i), f(x_j))| \forall x_i, x_j \in X$ and is given by eq. 1.

$$S_{IDMAP} = \frac{\delta(x_i, x_j) - \delta_{\min}}{\delta_{\max} - \delta_{\min}} - d(y_i, y_j)$$

Results and Discussion

Monitoring Electrode Functionalization with Nanostructured Films.

Optimization of SAM fabrication was performed based on the cyclic voltammetry results in Figure S1 in the Electronic Supplementary Information where the $[Fe(CN)_6]^{-3}/[Fe(CN)_6]^{-4}$ redox process was monitored. This process leads to reduction and oxidation peaks at 108 and 341mV, respectively, for the Au surface. The adsorption of an 11-MUA monolayer on the Au surface decreases electron exchange between the electrode and $[Fe(CN)_6]^{-3}/[Fe(CN)_6]^{-4}$ solution, thus limiting diffusion of the electroactive species and decreasing the current density in the redox peaks. This charge exchange becomes less pronounced for electrodes modified during 8h or more, i.e. this is the time required to cover the gold electrode surface. The 11-MUA coating was confirmed in the AFM images of Figure S2, which also show that the roughness of the sensing film varies with the deposition of the active layer of anti-CA19-9 and then with the adsorption of CA19-9 mimicking a sensing experiment. More specifically, the root mean square roughness of the 11-MUA film was 5.1 nm, which increased to 13.9 with the layer of anti-CA19-9 antibodies and then to 16.9 nm after adsorption of CA19-9 molecules at high concentration.

The sensing mechanism, believed to be associated with specific adsorption of CA19-9 molecules on the anti-CA19-9 layer, can actually be interrogated with PM-IRRAS, where the spectrum of the matrix (architecture 11-MUA/EDC/NHS) to immobilize anti-CA19-9 antibodies is used as reference. Figure 2 shows a specific region of the PM-IRRAS spectra (see the entire spectra in Figure S3, and the procedure for baseline correction in Figure S4 in the Electronic Supplementary Material), with bands at 1550 cm^{-1} and 1655 cm^{-1} assigned to amide II and amide I groups[33,34] present in both antibodies (anti-CA19-9) and antigens (CA19-9). The area and intensity of these bands increase with CA19-9 concentration, as expected. This can be seen in Figures S5 and S6 in the Electronic Supplementary Material for the bands assigned to amide groups, including C=O stretching, C-N stretching, and N-H bond[33,34].

View Article Online
DOI: 10.1039/C8AN00430G

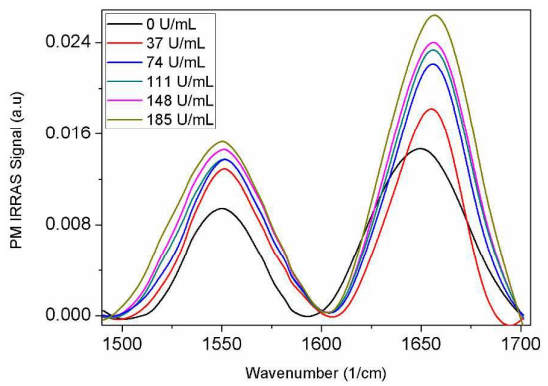

Figure 2: PM-IRRAS spectra of 11-MUA/EDC/NHS film modified with antibodies and different concentrations of CA19-9 biomarkers. The spectrum for the architecture 11-MUA/EDC/NHS was used as baseline.

Detection of CA19-9 Protein

The kinetics of adsorption of CA19-9 biomarkers on the immunosensor was studied to determine the optimized conditions for the experiments with distinct biomarker concentrations. Figure 3 shows the capacitance spectra obtained with the immunosensor (11-MUA/EDC/NHS/anti-CA19-9) exposed to a 37 U/mL concentration of CA19-9 at various adsorption times. The increased adsorption can be represented by plotting the capacitance at a fixed frequency (we chose 1 kHz) versus time of adsorption, where the capacitance no longer increases above 48.24 nF according to the figure in the insert. This time dependence can be modeled with a double Langmuir-Freundlich function[18], which may represent two adsorption processes of CA19-9 biomarker on the interdigitated electrodes modified with 11-MUA/EDC/NHS/anti-CA19-9. Also inferred from the figure is that 8 min is the minimum time for reaching complete adsorption at a given CA19-9 concentration, and this was the adsorption time employed for the subsequent sensing experiments.

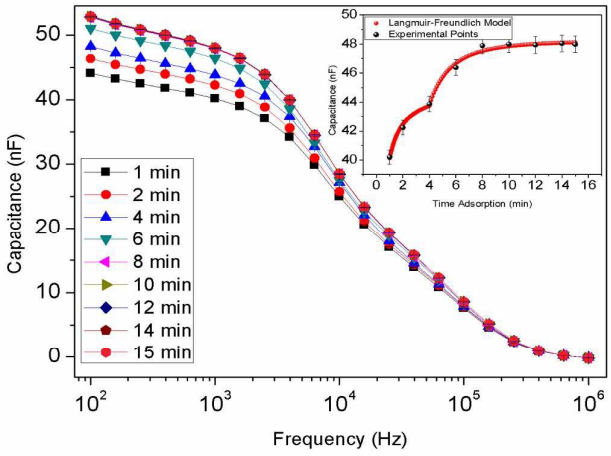

Figure 3: Capacitance spectra taken at different adsorption times for CA19-9 biomarker on immunosensors made with 11-MUA/EDC/NHS/anti-CA19-9. The insert shows the time dependence for the capacitance at 1 kHz, fitted with a double Langmuir-Freundlich equation.

Detection of CA19-9 commercial samples in PBS, supernatant cell samples (HT-29 and SW-620), and CA19-9 immersed in FBS (12.26 U/mL) was performed with impedance spectroscopy, thus generating the capacitance spectra in Figure 4. Changes in the spectra are more prominent at intermediate (1-10 kHz) and low frequency regions (0.1-1 kHz), because the sensor response is governed by specific interaction of the CA19-9 biomarker with the antibody immobilized on the electrode and the ensuing effect on the electrical double layer[35,36] induced by such specific interactions. The increase in capacitance at 1 kHz with CA19-9 concentration in the insert of Figure 4 can be fitted with a combination of Langmuir-Freundlich functions as in Eq. 2.

$$q = \frac{Q_{sat1}(K_{a1}C)^{n1}}{1+(K_{a1}C)^{n1}} + \frac{Q_{sat2}(K_{a2}C)^{n2}}{1+(K_{a2}C)^{n2}} \quad (2)$$

where q is amount of adsorbed material on the substrate at equilibrium, Q_{sat1} and Q_{sat2} are adsorption capacities related to the number of available active sites, C is the analyte concentration at equilibrium, K_{a1} and K_{a2} are affinity constants for adsorption, and n_1 and n_2 are heterogeneity indices. The choice of 1 kHz as the frequency for this analysis was based on a subsidiary study in which the parallel coordinates technique was used to plot the capacitance data (see Figure S7 in the Electronic Supplementary Information), and from which we determined the highest silhouette coefficient for distinguishing similar samples[32].

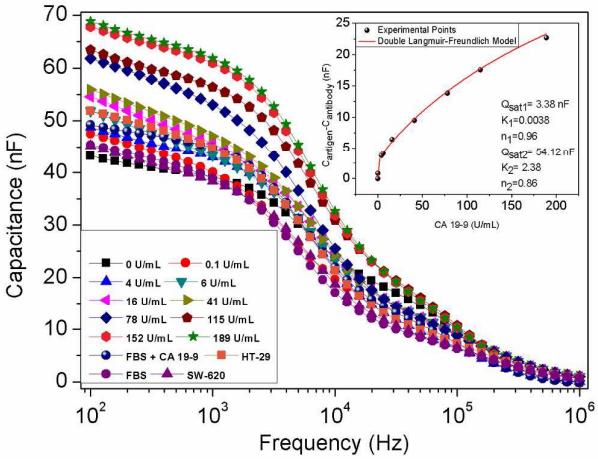

Figure 4: Capacitance spectra for 11-MUA/EDC/NHS/anti-CA19-9 immunosensor immersed in PBS solutions with various concentrations of CA19-9 commercial samples, cell supernatant samples (HT-29 and SW-620) and CA19-9 commercial sample immersed in FBS (12.26 U/mL). The insert shows the CA19-9 concentration dependence for the

View Article Online
DOI: 10.1039/C8AN00430G

capacitance at 1 kHz, which can be fitted with a double Langmuir-Freundlich function.

The reason why there are two Langmuir-Freundlich processes, rather than one as is common in other immunosensors, cannot be determined with the present data. It is nevertheless consistent with the two-process fitting for the kinetics of adsorption in the inset of Figure 3. It may seem surprising that the simple Langmuir-Freundlich model should account for the changes in electrical response where many intermolecular interactions are involved. We speculate that this occurs because of the predominance of the antigen-antibody interactions, which are so strong to make all the other interactions irrelevant when modeling the concentration dependence of the electrical response. Since the plot in the insert of Figure 4 is not linear, we took an extrapolation of the low concentration region and used the IUPAC method to determine the limit of detection of 0.68 U/mL, which is comparable to similar immunosensors[16] and competitive with Elecsys commercial tests[37]. Significantly, this level of sensitivity is sufficient for clinical diagnosis since the reference value for patients with pancreatic cancer is 37 U/mL[38,39]. Furthermore, supernatant of HT-29 cells and CA19-9 immersed in FBS (12.26 U/mL) were considered similar to commercial samples from the 6-16 U/mL region, while the SW-620 supernatant cells and FBS samples showed similarity to samples from the 0-0.1 U/mL region. The quantifications of these samples using electrochemiluminescence are given in Table S2 in the Electronic Supplementary Material.

The excellent performance in detecting CA19-9 in cell supernatant and in protein immersed in FBS samples served as motivation to investigate whether the immunosensor would also be capable of distinguishing samples of human blood serum from eight patients (Ethics Committee Number: 1.447.041). This was done by projecting the capacitance spectra using the IDMAP technique, with which similar spectra should be projected close to each other on the 2D IDMAP plot. Figure 5 indeed shows clear distinction for the blood serum with different CA19-9 concentrations. More importantly, the group of patients with CA19-9 concentration above 37U/mL is clearly discriminated.

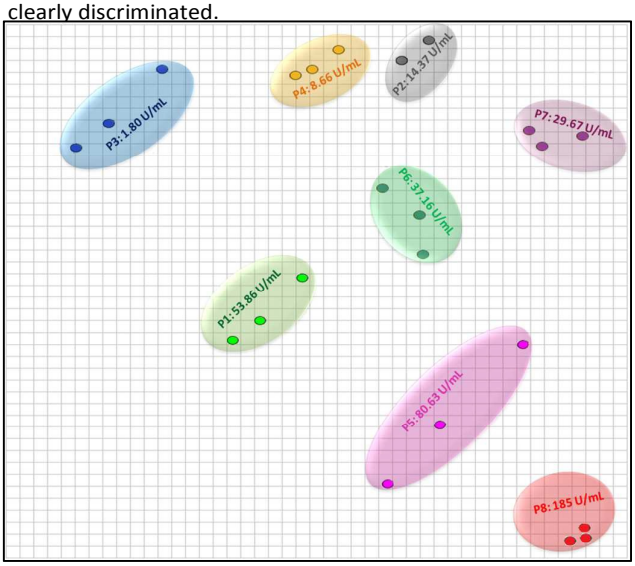

Figure 5: Capacitance data in triplicate projected on an IDMAP plot, which were obtained from sensing experiments with blood serum samples from eight patients (labeled as P1 through P8). The clusters were established from measurements in blind tests. The labels with the concentrations obtained in electrochemiluminescence immunoassays (ECLIA), as described in the Experimental Section, were included at the end of the plotting procedure.

In addition to reaching a high sensitivity, one of the most important features of immunosensors is selectivity, in order to avoid false positives (or false negatives). We tested the selectivity of the 11-MUA/EDC/NHS/anti-CA19-9 immunosensor in two types of control experiments. Figure S8 in the Supplementary Material shows that the capacitance at a fixed frequency is not altered upon changing the concentration of CA19-9 biomarker when the sensing unit does not contain an active layer of anti-CA19-9 antibodies, in contrast to the expected increase in capacitance for the immunosensor made with such an active layer. In the second type of control experiments, the immunosensor was exposed to cell supernatants samples (HT-29 and SW-620), analytes present in blood including ascorbic acid (AA), uric acid (UA), and fetal bovine serum (FBS), in addition to another biomarker for HIV (p24). Figure 6 shows the IDMAP plot for the capacitance spectra. On the right hand side are the samples with no (or very small) CA19-9 concentrations, including the buffer solutions, commercial samples, the non-specific analytes and the SW620 cells. The samples containing CA19-9 are placed progressively to the left as the protein concentration increases.

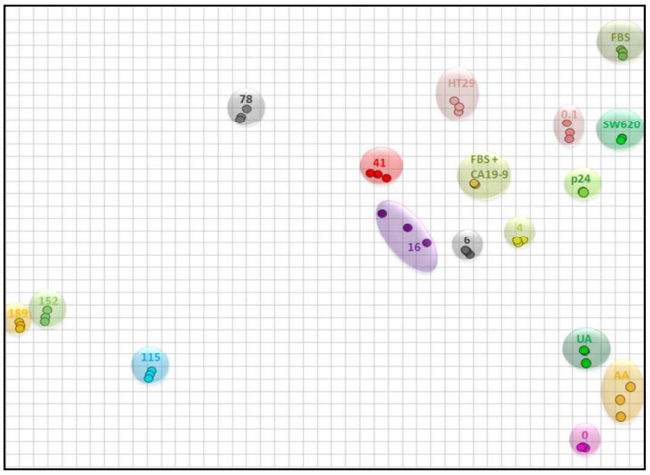

Figure 6: IDMAP for the capacitance spectra of CA19-9 commercial samples, cell supernatants (HT-29 and SW-620), CA19-9 immersed in fetal bovine serum (FBS), and non-specific analytes (AU, AA, p24). The data for the blood serum samples shown in Figure 5 were not included in this figure because the electrical response of the serum samples differs considerably and the corresponding data points would be positioned far away from the other data points

View Article Online
DOI: 10.1039/C8AN00430G

Conclusions

A relatively simple film architecture has been used to fabricate immunosensors to detect the biomarker CA19-9, using Electrical Impedance Spectroscopy. This detection method is advantageous because it allows for electrode miniaturization, no need to employ electroactive molecules and reference electrodes. Though the immunosensor had only a self-assembled monolayer coated with the active layer of anti-CA19-9 antibodies, being simpler than in previous works, it was sufficiently sensitive with a limit of detection of 0.68 U/mL in order to apply for early diagnosis of pancreatic cancer. In addition, by treating the capacitance data with multidimensional projection techniques, it has been possible to discriminate blood serum samples from patients which had distinct concentrations of CA19-9. Indeed, these experiments served as a proof-of-principle that patients likely to develop (or already developed) pancreatic cancer could be diagnosed in a simple, fast screening procedure.

The results from a series of control experiments confirmed the immunosensor robustness, with no false positives, proving that the high sensitivity arises solely from the antibody-antigen interaction. This interaction was actually investigated in detail using PM-IRRAS and verifying that the concentration dependence for the change in capacitance obeys a Langmuir-Freundlich model with two combined functions. Together with reports from the recent literature, the results shown here confirm that the technology of immunosensors based on impedance spectroscopy is mature for introducing detection of CA19-9 in routine clinical practice. There are, however, important challenges to be faced before this type of immunosensor can be widely disseminated. The first challenge is associated with the required mass production of reproducible sensing units (test stripes), which can only be achieved with a systematic, diligent device engineering work. However, even with such a work it is probably not possible to fabricate sensing units with identical electrical responses – unlike the case of devices made with inorganic semiconductors. The task of establishing reliable detection ranges and calibration is therefore essential. The second challenge arises from the need of data analysis. If multidimensional projections are to be used, for example, different mappings will be generated when sensing units are replaced, so that some sort of calibration will be necessary. This has to be done via data processing with software to avoid extensive measurements to establish standards. A solution to this problem is not yet available, thus requiring integrated research by computer scientists and analytical chemists.

Conflicts of Interest

There are no conflicts to declare.

Acknowledgments

The authors thank CAPES, FAPESP (Grant 2013/14262-7 and 2012/15543-7), CNPq (150985/2017-7), nBioNet network and Barretos Cancer Hospital for the financial support. Acknowledgments are also given to Daniel Segura (danielfsegura@outlook.com) for the artwork.

Bibliographic References & Notes

1 R. Blum and Y. Kloog, *Cell Death Dis.*, 2014, **5**, e1065–e1065.
2 S. Scarà, P. Bottoni and R. Scatena, in *Advances in Cancer Biomarkers*, ed. R. Scatena, Springer Netherlands, Dordrecht, 2015, vol. 867, pp. 247–260.
3 Q. Meng, S. Shi, C. Liang, D. Liang, W. Xu, S. Ji, B. Zhang, Q. Ni, J. Xu and X. Yu, *OncoTargets Ther.*, 2017, **10**, 4591–4598.
4 J. Wang, *Biosens. Bioelectron.*, 2006, **21**, 1887–1892.
5 J. C. Soares, F. M. Shimizu, A. C. Soares, L. Caseli, J. Ferreira and O. N. Oliveira, *ACS Appl. Mater. Interfaces*, 2015, **7**, 11833–11841.
6 J. C. Soares, A. C. Soares, P. A. R. Pereira, V. da C. Rodrigues, F. M. Shimizu, M. E. Melendez, C. Scapulatempo Neto, A. L. Carvalho, F. L. Leite, S. A. S. Machado and O. N. Oliveira, *Phys. Chem. Chem. Phys.*, 2016, **18**, 8412–8418.
7 M. Komiyama, K. Yoshimoto, M. Sisido and K. Ariga, *Bull. Chem. Soc. Jpn.*, 2017, **90**, 967–1004.
8 K. Ariga, K. Minami and L. K. Shrestha, *The Analyst*, 2016, **141**, 2629–2638.
9 S. Acharya, J. P. Hill and K. Ariga, *Adv. Mater.*, 2009, **21**, 2959–2981.
10 K. Ariga, Y. Yamauchi, G. Rydzek, Q. Ji, Y. Yonamine, K. C.-W. Wu and J. P. Hill, *Chem. Lett.*, 2014, **43**, 36–68.
11 G. Decher, J. D. Hong and J. Schmitt, *Thin Solid Films*, 1992, **210–211**, 831–835.
12 G. Rydzek, Q. Ji, M. Li, P. Schaaf, J. P. Hill, F. Boulmedais and K. Ariga, *Nano Today*, 2015, **10**, 138–167.
13 R. Narayan, *Nanobiomaterials: nanostructured materials for biomedical applications*, Woodhead Publishing, Duxford, UK, 2018.
14 S. Casalini, C. A. Bortolotti, F. Leonardi and F. Biscarini, *Chem. Soc. Rev.*, 2017, **46**, 40–71.
15 G. Decher and J. B. Schlenoff, Eds., *Multilayer thin films: sequential assembly of nanocomposite materials*, Wiley-VCH, Weinheim, 2012.
16 A. C. Soares, J. C. Soares, F. M. Shimizu, M. E. Melendez, A. L. Carvalho and O. N. Oliveira, *ACS Appl. Mater. Interfaces*, 2015, **7**, 25930–25937.
17 A. Thapa, A. C. Soares, J. C. Soares, I. T. Awan, D. Volpati, M. E. Melendez, J. H. T. G. Fregnani, A. L. Carvalho and O. N. Oliveira, *ACS Appl. Mater. Interfaces*, 2017, **9**, 25878–25886.
18 J. C. Soares, L. E. O. Iwaki, A. C. Soares, V. C. Rodrigues, M. E. Melendez, J. H. T. G. Fregnani, R. M. Reis, A. L. Carvalho, D. S. Corrêa and O. N. Oliveira, *ACS Omega*, 2017, **2**, 6975–6983.

View Article Online
DOI: 10.1039/C8AN00430G

19 Z. Huang, Z. Jiang, C. Zhao, W. Han, L. Lin, A. Liu, S. Weng and X. Lin, *Int. J. Nanomedicine*, 2017, **Volume 12**, 3049–3058.
20 C. K. Tang, A. Vaze and J. F. Rusling, *Anal Methods*, 2014, **6**, 8878–8881.
21 V. da C. Rodrigues, C. H. Comin, J. C. Soares, A. C. Soares, M. E. Melendez, J. H. T. G. Fregnani, A. L. Carvalho, L. da F. Costa and O. N. Oliveira, *ACS Appl. Mater. Interfaces*, 2017, **9**, 5885–5890.
22 C. Zong, J. Wu, C. Wang, H. Ju and F. Yan, *Anal. Chem.*, 2012, **84**, 2410–2415.
23 L. Loo, J. A. Capobianco, W. Wu, X. Gao, W. Y. Shih, W.-H. Shih, K. Pourrezaei, M. K. Robinson and G. P. Adams, *Anal. Chem.*, 2011, **83**, 3392–3397.
24 M. Yang, X. Yi, J. Wang and F. Zhou, *The Analyst*, 2014, **139**, 1814.
25 W.-C. Law, K.-T. Yong, A. Baev and P. N. Prasad, *ACS Nano*, 2011, **5**, 4858–4864.
26 S. Ishihara, J. Labuta, W. Van Rossom, D. Ishikawa, K. Minami, J. P. Hill and K. Ariga, *Phys. Chem. Chem. Phys.*, 2014, **16**, 9713.
27 F. M. Shimizu, F. R. Todão, A. L. Gobbi, O. N. Oliveira, C. D. Garcia and R. S. Lima, *ACS Sens.*, 2017, **2**, 1027–1034.
28 M. L. Moraes, L. Petri, V. Oliveira, C. A. Olivati, M. C. F. de Oliveira, F. V. Paulovich, O. N. Oliveira and M. Ferreira, *Sens. Actuators B Chem.*, 2012, **166–167**, 231–238.
29 F. V. Paulovich, M. L. Moraes, R. M. Maki, M. Ferreira, O. N. Oliveira Jr. and M. C. F. de Oliveira, *The Analyst*, 2011, **136**, 1344.
30 A. Riul Jr., C. A. R. Dantas, C. M. Miyazaki and O. N. Oliveira Jr., *The Analyst*, 2010, **135**, 2481.
31 F. V. Paulovich, R. M. Maki, M. C. F. de Oliveira, M. C. Colhone, F. R. Santos, V. Migliaccio, P. Ciancaglini, K. R. Perez, R. G. Stabeli, Â. C. Perinoto, O. N. Oliveira and V. Zucolotto, *Anal. Bioanal. Chem.*, 2011, **400**, 1153–1159.
32 A. Inselberg and B. Dimsdale, IEEE Comput. Soc. Press, 1990, 361–378.
33 N. B. Colthup, L. H. Daly and S. E. Wiberley, *Introduction to infrared and Raman spectroscopy*, Academic Press, Boston, 3rd ed., 1990.
34 A. Więckowski, C. Korzeniewski and B. Braunschweig, Eds., *Vibrational spectroscopy at electrified interfaces*, Wiley, Hoboken, New Jersey, 2013.
35 E. Barsoukov and J. R. Macdonald, Eds., *Impedance spectroscopy: theory, experiment, and applications*, Wiley-Interscience, Hoboken, N.J, 2nd ed., 2005.
36 V. F. Lvovich, *Impedance spectroscopy: applications to electrochemical and dielectric phenomena*, Wiley, Hoboken, N.J, 2012.
37 R. Passerini, D. Riggio, M. Salvatici, L. Zorzino, D. Radice and M. T. Sandri, *Clin. Chem. Lab. Med.*, 2007, **45**, 100-104.
38 Y.-L. Chen, C.-H. Chen, R.-H. Hu, M.-C. Ho and Y.-M. Jeng, *Sci. World J.*, 2013, **2013**, 1–6.
39 Q. Wang, Z. Ji, Z. Chen, H. Li, H. Fan, X. Fan, B. Shi and Y. Fang, *Int. J. Surg.*, 2015, **15**, 113–116.